X. Zheng

Q. Xue

R. Mittal[1]
Professor
e-mail: mittal@jhu.edu

Department of Mechanical Engineering,
Johns Hopkins University,
Baltimore, MD 21218

S. Beilamowicz
Division of Otolaryngology,
George Washington University,
Washington, DC 20052

A Coupled Sharp-Interface Immersed Boundary-Finite-Element Method for Flow-Structure Interaction With Application to Human Phonation

A new flow-structure interaction method is presented, which couples a sharp-interface immersed boundary method flow solver with a finite-element method based solid dynamics solver. The coupled method provides robust and high-fidelity solution for complex flow-structure interaction (FSI) problems such as those involving three-dimensional flow and viscoelastic solids. The FSI solver is used to simulate flow-induced vibrations of the vocal folds during phonation. Both two- and three-dimensional models have been examined and qualitative, as well as quantitative comparisons, have been made with established results in order to validate the solver. The solver is used to study the onset of phonation in a two-dimensional laryngeal model and the dynamics of the glottal jet in a three-dimensional model and results from these studies are also presented.

[DOI: 10.1115/1.4002587]

Keywords: immersed boundary method, finite-element method flow-structure interaction, phonation, flow-induced vibration

1 Introduction

Flow-structure interaction (FSI), which refers to the interaction of a moveable and/or deformable structure with an internal surrounding fluid, occurs in a number of systems in the human body and is oftentimes critical to the physiology of the system. One obvious example is the cardiovascular system, where the pumping of blood from the heart is the result of deformation of the heart wall and the functioning of the heart valves is mostly driven by flow-structure interaction. Flow-structure interaction is also the key to the physiology of the gastrointestinal system, where peristalsis is employed to move food, as well as the respiratory system, where contraction/expansion of the lungs leads to respiration.

Another system where FSI is critical is the phonatory system, where airflow induced vibration of the vocal folds in the larynx leads to the production of sound, i.e., to phonation. This system is the primary focus of the current work wherein we are working toward constructing high-fidelity computational tools that model the biomechanics of phonation. The motivation is that such tools will allow us to better understand the fundamental physical mechanisms that underlie phonation. Eventually, such tools could be used for preoperative assessment of laryngeal disorders that affect speech and even for surgical planning.

Significant advances have been made in the development of methods for simulating flow-structure interaction in physiological systems. One class of commonly used methods is the so-called arbitrary-Lagrangian–Eulerian (ALE) methods where the Lagrangian formulation of the Navier equation for solid dynamics is solved in a coupled manner with the Eulerian formulation of the Navier–Stokes equation for flow. The vast majority of commercial FSI software employ the ALE method, and these have been used extensively in the biomedical research especially in the cardiovascular modeling [1–7]. However, the ALE method requires the simulation to be carried out on a body-conformal mesh, which has to be modified via a suitable remeshing algorithm at every time-step. Cases involving large-deformation and/or topological changes of the boundary pose a severe challenge for the remeshing procedure. Furthermore, the unstructured nature of the mesh eliminates the use of powerful line-iterative and geometric multigrid techniques for the sparse-systems that are required to be solved. Additionally, in order to provide robustness in the presence of distorted grids, the ALE based solvers also employ numerical dissipation through "upwinding," "stabilizers," or addition of "artificial-viscosity," which tends to diminish natural flow instabilities, spuriously damp vortex structures, and hide the effects of under-resolution.

An alternate approach is to employ an immersed boundary method (IBM) for the flow simulation. This type of method was initially developed by Peskin [8] to simulate cardiovascular dynamics and this method and its variants (including the so-called fictitious domain method) have since been used for a variety of flow problems in engineering and biomechanics [9–15]. In this type of method, the governing equations are solved on a fixed Cartesian grid, which does not conform to the solid boundaries, and this essentially eliminates the grid remeshing issues encountered with body-conformal grid methods. The structured nature of the mesh also allows for the use of powerful line-iterative schemes as well as geometric multigrid methods, which can provide rapid solution of the discretized equations. However, in this type of method, a discrete delta function forcing term used to model the effect of the boundary is spread across multiple grid cells near the boundary and consequently produces a "diffuse" fluid-solid interface. This diminishes the resolution of the boundary layer and associated vortex dynamics and this can be undesirable at higher Reynolds numbers.

We have recently developed a highly versatile immersed boundary method for simulating flow with complex moving/deforming boundaries [16]. This method employs a multidimen-

---

[1] Corresponding author.

Contributed by the Bioengineering Division of ASME for publication in the Journal of Biomechanical Engineering. Manuscript received September 24, 2009; final manuscript received September 2, 2010; accepted manuscript posted September 21, 2010; published online October 15, 2010. Assoc. Editor: Victor H. Barocas.

sional ghost-cell methodology in conjunction with a finite difference scheme to solve the 3D, unsteady, incompressible Navier–Stokes equations on a Cartesian grid. This methodology is categorized as being a "sharp-interface" method in that the imposition of the no-slip, no-penetration boundary condition is localized precisely on the immersed boundary and is not spread (or diffused) artificially into the neighborhood of the boundary [11]. The method also ensures second-order global and local spatial accuracy, and this, along with the sharp-interface treatment, provides for accurate modeling of the boundary layer. This method is nondissipative and energy conserving, which is highly sensitive to grid resolution, does not damp out natural flow instabilities, and does not spuriously damp out vortex structures.

The flow solution is only one-half of the FSI problem. Also needed is an appropriate technique for solving the solid dynamics, as well as a way of coupling the two solution procedures. There are a number of approaches available for modeling the solid dynamics as well as for coupling the solid and fluid phases in the computation. For instance, Luo et al. [17] developed a Cartesian grid based immersed boundary method to solve the Navier equations for a viscoelastic solid and coupled it to the immersed boundary solver of Mittal et al. [16]. The use of a Cartesian mesh simplifies the mesh generation problem significantly, and this is the primary advantage of this method. The solid and the fluid use different Cartesian meshes, and these provide flexibility in choosing a grid resolution that is appropriate for each phase. However, the method is designed for small solid deformation and is not easily extendable to large-deformation problems, which are routinely encountered in biomechanics.

More recently, Zhao et al. [18] developed a Cartesian grid based method that solves FSI problems in a fully coupled manner. A single set of equations is solved on a single Cartesian grid that covers both the solid and fluid phases, wherein body force terms are used to model the elastic forces inside the fluid. The coupling between fluid and solid effected via transferring of surface stresses from the solid to the fluid. This approach has the advantage that it can address large-deformation problems. However, as mentioned before, the method uses a single Cartesian mesh for solving both the solid and the fluid. While this simplifies the computational methodology, it does not allow much flexibility in separately choosing the grid resolution for the fluid and solid phases. This flexibility is important if one would like to address a large variety of FSI problems. Depending on the rigidity and other material constraints, the resolution requirements for the solid dynamics can be very different from that of the fluid flow. Furthermore, many solids, particularly those encountered in biology can have multilayered, nonisotropic, nonhomogeneous structures, which require special attention to the grid resolution. For instance, the vocal folds have a three-layered structure [19], which consists of a thin outer layer (lamina propria), an intermediate ligament layer, and the internal muscle (vocalis) and appropriate resolution of each of these layers is required. Similarly, sometimes the flow may require significantly higher resolution than the solid due to, for instance, the presence of thin boundary layers.

For such general FSI problems, a methodology is needed, which allows more flexibility in choosing the grid resolution for the solid and fluids phases and also has the potential of being extended to large-deformation problems. The finite-element method is the de facto standard for modeling in solid dynamics. This method has been extensively used for a variety of solid dynamics problems and the limitations and capabilities of these methods are well understood [20]. It would therefore seem that an immersed boundary solver (for the fluid) coupled with a finite-element solver (for the solid) would provide all the requisite capabilities for addressing a wide variety of FSI problems in biomechanics.

Motivated by this, we have coupled the sharp-interface immersed boundary method with a finite-element solver that is capable of solving for the deformation in viscoelastic solids. Since most biological materials show some degree of viscoelasticity, including this capability is essential for these types of applications. The FE solver is coupled to the IB fluid solver via an explicit coupling scheme that is shown to be adequate for air-tissue interaction problems encountered in phonation and respiration. Furthermore, the current formulation is limited to small deformation but the underlying finite-element and fluid-solid coupling methodologies could be extended to large deformations.

In the current paper, we present the salient features of the computational methodology. Following this, we describe the use of the method for a two-dimensional model of the human larynx. The model is used to explore a number of issues associated with the biomechanics of phonation including phonation onset, glottal jet dynamics, and vocal fold stresses. Comparisons of computed results to existing data on phonation are made, wherever possible. Finally, we show results from a 3D model of the human larynx, which demonstrates the ability of the solver to eventually address more realistic laryngeal models.

2 Numerical Method

In this section, we describe the key elements of the numerical method that we have developed here including the immersed boundary flow solver, the finite-element viscoelastic structural solver, and the flow-structure coupling approach.

3 Immersed Boundary Flow Solver

The governing equations are the 3D, unsteady, incompressible Navier–Stokes equations written in the primitive variable form

$$\frac{\partial u_i}{\partial x_i} = 0 \tag{1}$$

$$\frac{\partial u_i}{\partial t} + \frac{\partial u_i u_j}{\partial x_j} = -\frac{1}{\rho}\frac{\partial p}{\partial x_i} + \nu \frac{\partial^2 u_i}{\partial x_j \, \partial x_j} \tag{2}$$

where u_j are velocity components in three directions, p is pressure, and ρ and υ are flow density and kinematic viscosity.

The Navier–Stokes equations are discretized in space using a cell-centered collocated (nonstaggered) arrangement of the primitive variables u_i and p. The fractional step method of Van Kan [21] is used to integrate the equations in time, which consists of three substeps. In the first substep, a modified momentum equation is solved to get an intermediate velocity u^*. A second-order Adams–Bashforth scheme is employed for the convective terms while the implicit Crank–Nicholson scheme is used to discretize the diffusion terms to eliminate the viscous stability constraint. The second substep requires the solution of the pressure correction equation, which is solved with a highly efficient geometric multigrid method. Once the pressure is obtained, the velocity field is updated to its final value.

The simulation employs a sharp interface immersed boundary method based on a multidimensional ghost-cell methodology, which has been described in detail in Mittal et al. [16]. In this method, the body whose surface is described by triangular elements is immersed into a Cartesian volume grid. As shown in Fig. 1, the Cartesian cells are solid cells or fluid cells depending on whether they are inside or outside the boundaries of the bodies. This ghost-cell method proceeds by identifying the ghost cells (denoted by GC), which are solid cells, which have at least one fluid cell neighbor. A "probe" is then extended from one of these ghost cells onto an "image-point" (denoted by IP) inside the fluid such that it intersects normal to immersed boundary and the boundary intercept (denoted by BI) is midway between the ghost-node and the image-point. Next, a bilinear interpolation (trilinear in 3D) is used to express the value of a generic flow variable at the image-point in terms of the surrounding nodes. Following this, the value of the variable at the ghost-cell is computed by using a central-difference approximation along the normal probe such that the prescribed boundary condition at the boundary intercept is

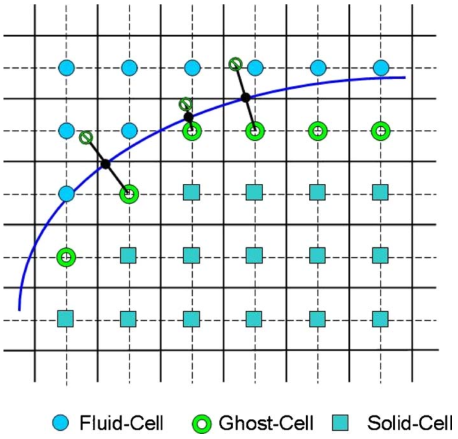

Fig. 1 2D schematic describing ghost-cell methodology

incorporated. Using this procedure, the boundary conditions are prescribed to the second-order accuracy, and this, along with the second-order accurate discretization of the fluid cells, leads to the local and global second-order accuracy in the computations. The formulation for Dirichlet and Neumann boundary conditions are shown as follows:

$$\phi_{\mathrm{IP}} = \sum \beta_i \phi_i \tag{3}$$

$$\phi_{\mathrm{GC}} + \sum \beta_i \phi_i = 2\phi_{\mathrm{BI}} \tag{4}$$

$$\phi_{\mathrm{GC}} - \sum \beta_i \phi_i = \Delta l \left(\frac{\delta \phi}{\delta n}\right)_{\mathrm{BI}} \tag{5}$$

where ϕ is the generic flow variable, i is from 1 to 4 (for 2D) or 8 (for 3D) and represents the ith surrounding node for IP, β is the interpolation weight, and Δl is the probe length.

Since the equations are written in the Eulerian form, boundary motion can now be included into this formulation by moving the boundary at a given time-step, recomputing the body-intercepts and image-points, and then advancing the flow equations in time. One issue associated with a moving boundary case of these types of methods is the so-called "fresh cell" problem [16,22], which refers to the cell that was solid cell at previous time-step and became fluid cell at current time-step due to the boundary motion. The method for treating such cell is described in detail in Mittal et al. [16] and will not be repeated here.

4 Viscoelastic Structural Modeling

The governing equations are the Navier equations written as

$$\rho \frac{\partial^2 d_i}{\partial t^2} = \frac{\partial \sigma_{ij}}{\partial x_j} + \rho f_i \tag{6}$$

where i and j range from 1 to 3, σ is the stress tensor, f_i is the body force component in i direction, ρ is the density, and d_i is the displacement component in i direction. Assuming a Kelvin–Voigt model [23] for the viscoelasticity, which has been extensively used in modeling tissue [23], the constitutive law between stress and strain can be written as

$$\sigma_{ij} = C_{ijkl}\varepsilon_{kl} + A_{ijkl}\dot{\varepsilon}_{kl} \tag{7}$$

where ε is the strain tensor, $\dot{\varepsilon}$ is the strain rate tensor, and C and A are fourth-order tensors corresponding to the material constants.

In the current method, a Galerkin formulation [20] is employed for the finite-element method. This well established [20] formulation employs virtual displacements to discretize Eq. (6) and represent it in terms of the nodal displacement as follows. The final result of this formulation is the following second-order ordinary differential equation for the nodal displacements:

$$M_{\alpha\beta}\ddot{D}^{\beta} + C_{\alpha\beta}\dot{D}^{\beta} + K_{\alpha\beta}D^{\beta} = F^{t}_{\alpha} + F^{b}_{\alpha} \tag{8}$$

where $M_{\alpha\beta}=\int_v \rho N_{j\beta} N_{i\alpha} dv$, $C_{\alpha\beta}=\int_v A_{ijkl} B_{kl\beta} B_{ij\alpha} dv$, and $K_{\alpha\beta} =\int_v C_{ijkl} B_{kl\beta} B_{ij\alpha} dv$ are the mass, damping, and stiffness matrices, respectively, and $F^{t}_{\alpha}=\int_{s\sigma} \sigma_s N_{i\alpha} ds$ and $F^{b}_{\alpha}=\int_v \rho f_i N_{i\alpha} dv$ are the nodal traction and nodal body force, respectively. In the above expressions, $N_{i\alpha}$ is a predefined weight (or "shape") function, which connects the displacement d_i at any arbitrary point inside an element through a weighted sum of the nodal displacement D^{α} as follows:

$$d_i = \sum_{\alpha=1}^{n} D^{\alpha} N_{i\alpha} \tag{9}$$

where n is the total number of nodes of the element (three for triangular and four for quadratic and tetrahedral elements). The M, K, and C matrices are obtained via an integration over the different elements. The integration is simplified through the use of isoparametric coordinates [20] Following this, Eq. (8) is dicretized in time using a Newmark scheme [20], leading to the following dicrete equation:

$$\left(K + \frac{1}{\beta \Delta t^2} M + \frac{\gamma}{\beta \Delta t} C\right) D^{n+1} = F^{n+1} + M\left[\frac{1}{\beta \Delta t^2} D^n + \frac{1}{\beta \Delta t}\dot{D}^n + \left(\frac{1}{2\beta} - 1\right)\ddot{D}^n\right] + C\left[\frac{\gamma}{\beta \Delta t} D^n + \left(\frac{\gamma}{\beta} - 1\right)\dot{D} + \left(\frac{\gamma}{2\beta} - 1\right)\Delta t \ddot{D}_n\right] \tag{10}$$

where β and γ are constants. We choose β=0.25 and γ=0.5, which results in a second-order accurate scheme in time. It should be noted that the Newmark scheme is unconditionally stable [20].

In order to reduce the memory requirement and improve the computational efficiency, a banded LU decomposition is employed to solve Eq. (10). Both Cuthill–Mckee [24] and Gibbs–Poole–Stockmeyer [25] methods are used to re-index the nodes and to find the smallest banded matrix.

Contact between bodies is a very common problem in mechanics. This phenomenon is particularly relevant to the problem of vocal fold vibration and phonation since the two vocal folds experience contact during each vibration cycle. In the current study, a penalty coefficient method [20] is used to model vocal fold contact. According to this method [20], the contact force is modeled as follows:

$$\boldsymbol{F}^{\mathrm{contact}} = \int \gamma g \, \boldsymbol{\nabla} g dA \tag{11}$$

where $\boldsymbol{F}^{\mathrm{contact}}$ is the contact force, A is the contact area, γ is the penalty coefficient (which is always positive), and g is the penetration distance. Thus, integrating the contact force over the contact area creates a contact force that opposes penetration of one vocal fold into another and is proportional to the penetration distance with γ as the constant of proportionality. This integration is performed using shape function N_a for each surface element, which intrudes into the contact plane. By choosing different values for γ, one can enforce different types of contact with higher values of γ, leading to a "harder" contact condition. It should be noted that high values of γ enhance the stiffness of the resulting system and can lead to additional constraints on the size of the time-step. In the normal phonation, the structure and movement of two vocal folds are nearly symmetric; thus, the contact almost occurs at the glottal center plane. In the current study, to simplify the situation, the contact condition is enforced on the glottal center plane (Fig. 2). It should be noted that in a more general case, which the contact does not necessarily occur on the center plane,

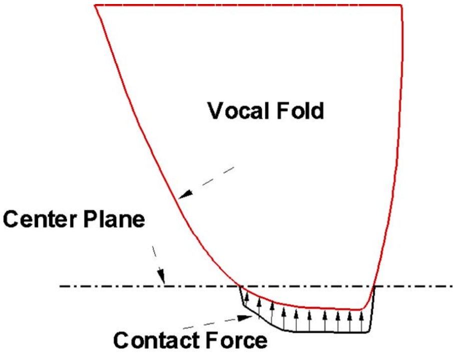

Fig. 2 2D illustration of contact force. The upper vocal fold intrudes into the center contact plane.

more sophisticated searching algorithms are required for the contact detection.

The finite-element solid solver has been validated for 2D and 3D canonical cases and the details for these tests can be found in Zheng [26].

5 Flow-Structure Coupling

A flow-structure coupling scheme has to be implemented through the surface mesh of the solid, which is comprised of triangular elements. For the flow solver, no-penetration, no-slip velocity boundary conditions are to be imposed [16]. According to the ghost-cell methodology described in the earlier section, these boundary conditions are applied at the boundary intercept points (IB). The locations and velocities at these points are directly interpolated from the surface nodal values of finite-element solution. For the solid solver, the traction has to be prescribed at the fluid-solid interface. The normal stress, as well as the shear stress, is computed using a trilinear interpolation (bilinear interpolation for 2D), which is described in Ghias et al. [27]. Once pressure and shear stress are computed at the surface nodal points, the total force on a given element is computed using the shape functions.

Usually, there are two coupling strategies for FSI, namely, loose coupling and strong coupling. The major difference between loose and strong couplings is that they, respectively, integrate the governing equations of structure explicitly and implicitly in time. The advantage of the strong coupling scheme is that it is robust and does not usually introduce stability constraints over and above those that exist for the flow and solid solvers. However, strong coupling usually requires an iterative procedure that can significantly increase the computational expense. On the other hand, loose coupling may be subject to additional stability constraints but is computational inexpensive. It should be noted that the flow solver used here employs explicit treatment of the convective terms and is therefore subject to CFL type time-step constraint [17]. This precludes the use of large time-steps and might eliminate the advantage of using a strong coupling scheme. If it can be shown that loose coupling will not lead to severe stability constraints for the problem at hand, then such a scheme would be ideal for our simulations. We now perform a heuristic assessment of the stability of the loose coupling scheme. For this analysis, we choose a flow configuration consisting of an elastically mounted sphere with negligible structural damping in a uniform potential flow. This canonical problem shares many of the features typical of FSI and the simplicity of the configuration makes it amenable to analysis (Fig. 3).

For the above configuration, an explicit coupling leads to the following equation for the motion of the structure in the streamwise direction:

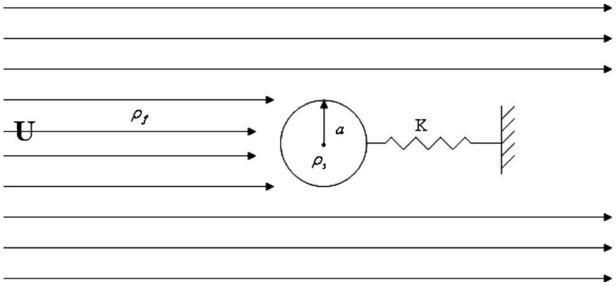

Fig. 3 Schematic flow past an elastically mounted sphere

$$M\ddot{X}^{n+1} + KX^{n+1} = F^n \tag{12}$$

where the fluid traction term F^n is computed using the previous time-step and X is the location of the center of the sphere. If the flow is assumed to be an incompressible potential flow, the fluid dynamic load on the sphere in the streamwise direction is given by [28]

$$F = -\tfrac{2}{3}\pi a^3 \rho_f(\dot{U}_B - \dot{U}) + \tfrac{4}{3}\pi a^3 \rho_f \dot{U} \tag{13}$$

where a is the radius of sphere, ρ_f is the fluid density, $\dot{U}_B = \ddot{X}$ is the body acceleration, and $\dot{U}$ is the free stream flow acceleration. The first term of Eq. (13) is the so-called added mass force, which is due to the sphere acceleration relative to the free stream. The second term is the force due to the imposed free stream pressure gradient. Assuming an explicit coupling between the flow and the solid, for a steady free stream, the equation of motion for the sphere becomes

$$\tfrac{4}{3}\pi a^3 \rho_s \ddot{X}^n + KX^n = -\tfrac{2}{3}\pi a^3 \rho_f \ddot{X}^{n-1} \tag{14}$$

where ρ_s is the solid density. Using a central-difference scheme for the acceleration terms, the resulting finite difference equation is

$$\frac{4}{3}\pi a^3 \rho_s \frac{X^{n+1} - 2X^n + X^{n-1}}{\Delta t^2} + KX^n = -\frac{2}{3}\pi a^3 \rho_f \frac{X^n - 2X^{n-1} + X^{n-2}}{\Delta t^2} \tag{15}$$

Assuming numerical error ε_n at time-step n propagates as $\varepsilon_n = \lambda \varepsilon_{n-1}$ leads to the following characteristic equation:

$$\lambda^3 + \left(\frac{1}{2}\frac{\rho_f}{\rho_s} + \Delta t^2 \omega^2 - 2\right)\lambda^2 + \left(1 - \frac{\rho_f}{\rho_s}\right)\lambda + \frac{1}{2}\frac{\rho_f}{\rho_s} = 0 \tag{16}$$

where $\omega = \sqrt{K/(4/3\pi a^3 \rho_s)}$ is the natural frequency of the system.

The critia for a stable solution is

$$|\lambda_i| \le 1 \quad \text{for } i = 1,2,3 \tag{17}$$

which leads to the following constraint for the roots of the cubic characteristic equation:

$$\left|\frac{1}{2}\frac{\rho_f}{\rho_s} + \Delta t^2 \omega^2 - 2\right| = |\lambda_1 + \lambda_2 + \lambda_3| \le 3 \tag{18}$$

$$\left|\frac{1}{2}\frac{\rho_f}{\rho_s}\right| = |\lambda_1 \lambda_2 \lambda_3| \le 1 \tag{19}$$

$$\left|1 - \frac{\rho_f}{\rho_s}\right| = |\lambda_1\lambda_2 + \lambda_2\lambda_3 + \lambda_1\lambda_3| \le 3 \tag{20}$$

These can be simplified to

$$\Delta t^2 \le \frac{1}{2\omega^2}\left(10 - \frac{\rho_f}{\rho_s}\right), \quad \frac{\rho_f}{\rho_s} \le 2, \quad \frac{\rho_f}{\rho_s} \le 4 \tag{21}$$

We are particularly interested in air-tissue interaction, so if we assume that the tissue has a density equivalent to water, then for

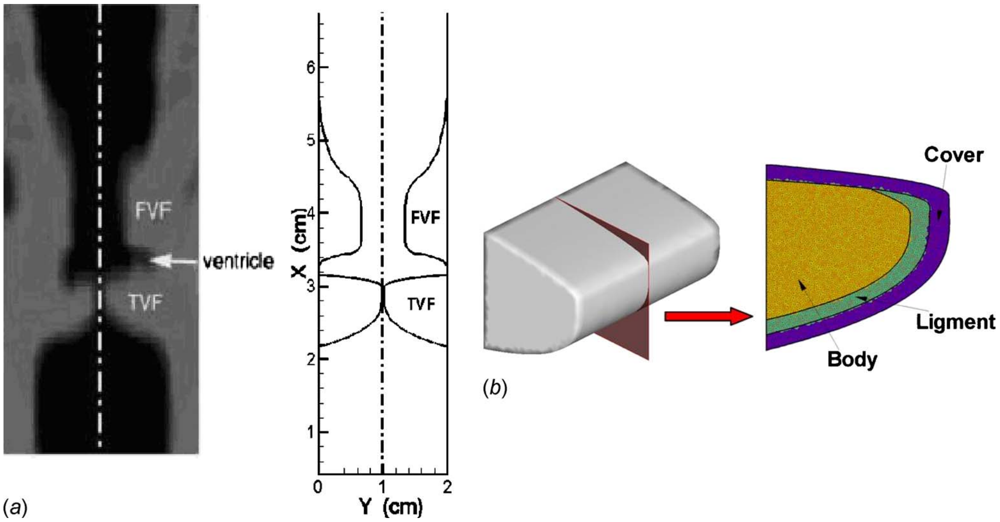

Fig. 4 (*a*) A coronal view of CT scan of human larynx and the current flow domain that attempts to match the key geometrical features in the CT scan. (*b*) Three-layer vocal fold inner structure inside an idealized geometric VF model based on CT scan and triangular elements used in the current solver.

air-tissue interaction, $\rho_f/\rho_s \equiv \rho_{\text{air}}/\rho_{\text{tissue}} \approx 1\ \text{kg/m}^3/1000\ \text{kg/m}^3 \sim 0.001$. Thus, the latter two conditions are easily satisfied. Furthermore, for air-tissue interaction, the first constraint becomes $\Delta t \leq \sqrt{5}/\omega$ or $\Delta t \leq 0.36\tau$, where τ is the time-period of the vibration. Given that we typically have O(1000) time-steps in each vibration cycle, the above condition is also satisfied quite easily. The above implies that the loose coupling scheme should work quite well for the air-tissue interaction problem associated with phonation. Note that the above analysis neglects viscosity, which could potentially modulate the stability behavior. However, given that viscosity would likely provide additional damping to the FSI system and that inviscid models have been used to predict basic features of FSI in phonation, we expect that an inviscid analysis will provide a reasonable assessment of the numerical stability.

In the explicit coupling scheme adopted here, the flow is marched by one step with the current deformed shape and velocities of the solid nodes as the boundary conditions. The aerodynamic forces imparted on the VF are then calculated at this current location of the vocal fold surface via an interpolation scheme on the flow grid. Finally, the equation for the solid is marched by one time-step with the updated surface traction, and the deformation and velocities on the solid grid are interpolated onto the vocal fold surface, so that the fluid/solid interface can be updated. This explicit coupling is quite simple, robust, and efficient. Implicit coupling can be easily implemented if needed by iterating between the fluid and solid solvers at each time-step.

6 Computational Modeling of Vocal Fold Dynamics During Phonation

The FSI method developed here has been employed to investigate the phonation problem, which results from a highly coupled biomechanical interaction between glottal airflow and vocal fold tissue. In the past few decades, scientists have achieved various degrees of success in modeling phonation. Approaches have included inviscid, irrotational flow models [29,30], lumped mass vocal fold models [29–32], and stationary [33] or specified vocal fold motion [34,35]. However, these models have inherently low-fidelity and able to capture limited characteristics of phonation. To provide quantitative results for direct clinical diagnosis and treatment, as well as the full understanding of the biophysics of phonation, a higher fidelity FSI computational model is required. This is the primary motivation for the current effort.

6.1 Model Setup. The dimension and geometry of the laryngeal model used here is based on a laryngeal CT scan of a 30 year old male shown in Fig. 4(*a*). The overall flow domain is a 12 cm long by 2 cm wide channel. The true vocal folds (TVFs) are 1 cm long and extend 0.99 cm toward the glottal midline. The false vocal folds (FVFs) are 2.3 cm long and extend 0.67 cm toward the supraglottal space. The ventricles are about 0.56 cm wide at their widest location, and the false vocal fold gap is 0.667 cm.

The FVFs are modeled as rigid bodies since they do not move during the normal phonation. The TVFs are viscoelastic bodies with a complex three-layer structure shown in Fig. 4(*b*). A 17,202 triangle mesh is used to represent the entire two-dimensional TVF. The material properties of each layer are given in Table 1. Similar properties were used in the past by Alipour et al. [36]. It should be noted that the longitudinal Young's modulus was not given by Alipour et al. [36] due to the in-plain motion assumption. It was shown by Cook et al. [37] that the longitude Young's modulus must be 10^4 times of in-plain Young's modulus to produce the equivalent vocal fold in-plain motion. Thus, in the current study, the longitudinal Young's modulus is set to be 10^4 times of in-plain Young's modulus. For the 2D simulation, a plain strain assumption has been adopted and the material is assumed to be isotropic with a Poisson's ratio of 0.3 [17].

For simulations of normal phonation, constant gauge pressures

Table 1 Material properties of the three-layers of the vocal folds

	ρ (g/cm^3)	E_p (kPa)	ν_p	E_{pz} (kPa)	ν_{pz}	G_{pz} (kPa)	η (P)
Cover	1.043	2.041	0.9	20,000	0.0	10	3
Ligament	1.043	3.306	0.9	33,000	0.0	40	5
Body	1.043	3.990	0.9	40,000	0.0	20	6

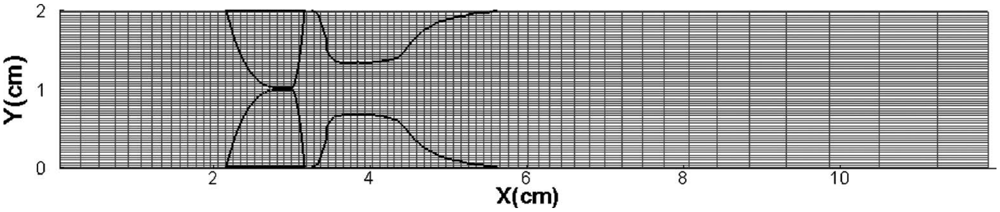

Fig. 5 Grid used in the current simulation. The figure shows every three grid points in each direction.

of 1 kPa and 0 kPa are applied at the inlet and exit of the domain, respectively, and these approximate typical physiological conditions. A homogeneous normal gradient velocity boundary condition is also applied at the inflow and outflow boundaries. Finally, no-slip and no-penetration boundary conditions are applied on the walls and the flow-tissue interfaces [38]. A 289×256 Cartesian grid is chosen for fluid mesh, which has a uniform grid in the y-direction and a nonuniform grid in the x-direction with a denser grid in the vicinity of TVFs and FVFs (as shown in Fig. 5).

In the simulation, a time-step corresponding to 3.5×10^{-3} ms is employed, which results in 1000–3000 time-steps in every vibration cycle for a typical phonation frequency between 100 Hz and 200 Hz. Three different studies are reported. The first two studies are based on a 2D laryngeal model and the primary motivation here is to validate computed results both qualitatively and quantitatively against established models and experiments. The grid employed in the 2D simulation is based on our past experience in simulating these flows and is subjected to grid refinement analysis in previous studies [17,39]. The third and final study is based on a 3D model of the vocal fold, where we demonstrate the ability of the current method to compute three-dimensional details of the vocal fold and glottal jet dynamics. The 2D simulations have been carried on a single-node of a 1.96 MHz AMD Opteron™ workstation, whereas the 3D simulations are performed on up to 128 processors of a Cray XT5.

6.2 Computational Study of Phonation Onset. We first present results from a phonation onset study, where the subglottal pressure is increased systematically from 0.1 kPa to 2.0 kPa (with intermediate values of 0.3 kPa, 0.5 kPa, 0.7 kPa, 1.0 kPa, and 1.5 kPa). It is well known that the onset of sustained vocal fold vibrations occurs via a Hopf's bifurcation [40] once the pressure exceeds a critical value, and we attempt to reproduce this phenomenon with the current computational model. The computations indicate no sustained vibrations for 0.1 kPa and 0.3 kPa cases, whereas all other cases exhibit such vibrations. Thus, the phonation onset threshold pressure is predicted to be between 0.3 kPa and 0.5 kPa. A similar range was reported by Baer [41], who conducted in vivo measurement on an excised larynx, as well as Titze et al. [42], who employed a computation with a two-mass vocal fold model coupled with a 1D Bernoulli equation. Thus, the current modeling procedure gives results that are inline with established studies.

For all of cases for which sustained vibrations are achieved, spectral analysis of the time-variation of the glottal gap-width is employed to extract the fundamental phonation frequency F_0. The variation of fundamental frequency F_0 versus subglottal pressure P_{sub} is shown in Fig. 6. Just above the threshold pressure, the fundamental frequency is found to increase nonlinearly with subglottal pressure but becomes nearly constant at higher subglottal pressures. It should be noted here that the experimental study of Titze et al. [42] indicates that the fundamental phonation frequency increases with subglottal pressure when the subglottal pressure is significantly larger than the normal phonation pressure. However, a pressure-frequency relationship similar to what is observed here was reported by Ishizaka [30] in one of his two-mass model FSI studies using a linear spring. Thus, it is quite likely that the reason that a behavior similar to Titze et al. [42] is not observed in the current simulations due to the assumption of material linearity. However, since the focus here is on investigating the normal phonatory behavior, we consider the current model adequate for this purpose.

6.3 Normal Phonation. In all of the current studies, the simulations were continued until the vocal fold vibration reached a stationary state with a limit-cycle type behavior. The characteristics of this stationary state are then examined to further establish the fidelity of the current modeling approach. Figure 7 shows the time history of the glottal airflow volume flux, which clearly shows that a stationary vibratory state has been established. The flux shows a phonation frequency of 231 Hz, which is at the upper end of the range associated with normal phonation in humans. The average and peak values of the computed volume flux rate are $0.01619\ \text{m}^2/\text{s}$ and $0.04328\ \text{m}^2/\text{s}$, respectively. If the vocal fold length is assumed to be 2 cm, which would be typical of an adult human, the average and peak volume fluxes are 322 ml/s and 865 ml/s, which are inline with in vivo measurement of excised larynges [43]. The typical value of the Reynolds number for human phonation is around 3000 based on the peak volume flux rate $\text{Re}_Q = (3/2)Q/\upsilon_a$, where υ_a is the kinematic viscosity of air. However, as shown in the previous study [17], the vibratory features of the vocal folds are relatively insensitive to the Reynolds number.

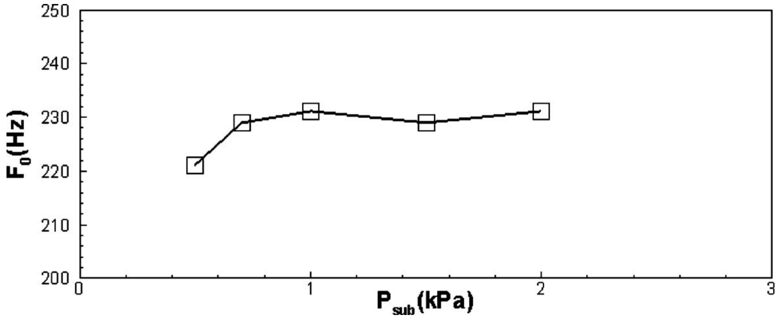

Fig. 6 Variation of fundamental frequency with subglottal pressure

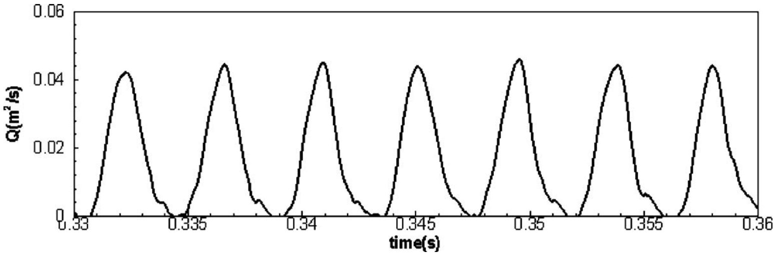

Fig. 7 Time variation of two-dimensional glottal volume fluxes in the stationary vibration stage

Thus, to alleviate the computational cost, the Reynolds numbers employed in the current study is reduced to 454 based on peak value of volume flux rate.

Figure 8 shows a sequence of instantaneous spanwise vorticity contours, which reveal the details of the flow dynamics during phonation. As the vocal folds open, the air is pushed out by the subglottal pressure into the supraglottal region, leading to the formation of the so-called glottal jet. The interesting thing is that the jet shows noticeable asymmetry and may be deflected to one side of the channel. This is a consequence of the strong flow recirculation zones in the supraglottal region created in previous cycles, which tend to deflect the incipient glottal jet in one direction or the other. The jet deflection is stochastic in nature and does not show any regular cycle-to-cycle behavior. This phenomenon of the so-called bimodal jet has been reported in several experimental studies [44–46], and further details of this phenomenon, along with the role of the false vocal folds in mitigating this bimodality, are described in Zheng et al. [39].

The mechanical stress in the vocal fold tissue is important since vocal folds may experience fatigue and damage due to the excessive localized stress, as well as due to cyclicality of the stress. In extreme cases, excessive and prolonged stress can cause laryngeal pathologies such as vocal fold nodules [47]. Thus, accurate computation of the stress inside the vocal folds can help shed insights into such laryngeal pathologies. In Fig. 9, we show contours of mechanical stress in the two vocal folds at two extreme positions during the vibration cycle. When the vocal folds are fully adducted, the contact between the vocal folds produces a large compressive stress (negative σ_{yy}) on the medial surfaces of the two vocal folds while at the same time, high levels of elongation stress (positive σ_{yy}) occur at the root of ligament and the maximum shear stress τ_{xy} occurs on the root of vocal folds. At the maximum abduction position, the shear stress becomes much smaller than during the closing phase. The normal stress σ_{yy} is mainly compressive during the opening phase and appears at the superior part of the vocal fold body. The normal stress σ_{xx} is similar at the two positions and is, in general, smaller than σ_{yy}.

7 3D Flow-Tissue Interaction

While the majority of computational laryngeal models employed in phonation studies are two-dimensional, the limitations of these models have been well recognized for some time. In particular, the 3D shape of the glottis and vocal folds are expected to have a significant effect on the vibratory dynamics, which cannot be captured in 2D models. Furthermore, 2D models cannot accurately compute the transition to turbulence also, which usually occurs in the glottal jet and which is expected to modify the flow characteristics significantly. In the current study, we have developed a relatively simple 3D model by extruding the 2D model 1.5 cm in anterior and posterior directions. The internal three-layer structure was kept identical along the longitudinal direction. The anterior, posterior, and lateral walls of true vocal folds were fixed to represent the attachment to the cartilage. A $12 \times 2.0 \times 1.5\ \text{cm}^3$ straight rectangular duct was used to mimic the human airway. The locations of vocal folds and false vocal folds inside the airway were kept the same as the 2D flow-tissue interaction study. The subglottal and supraglottal pressures were also kept the same as the 2D case, and no-slip boundary conditions are applied on all of the walls. This simulation employs a nonuniform $256 \times 128 \times 64$ Cartesian grid for the flow solver and a 58,427 tetrahedral element grid for the solid solver. While this

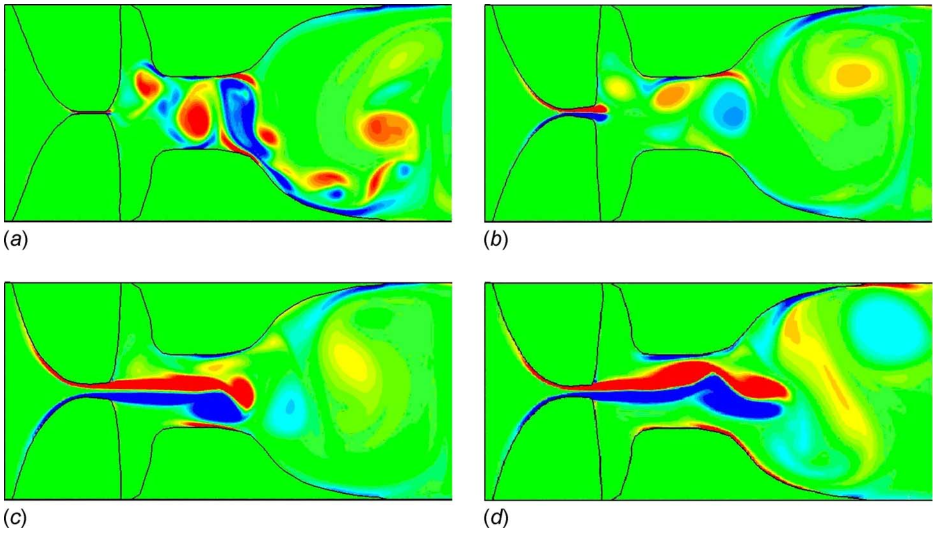

Fig. 8 Contours of spanwise vorticity during vocal fold vibration: (*a*) 0.3384 s, (*b*) 0.3398 s, (*c*) 0.3409 s, and (*d*) 0.3454 s

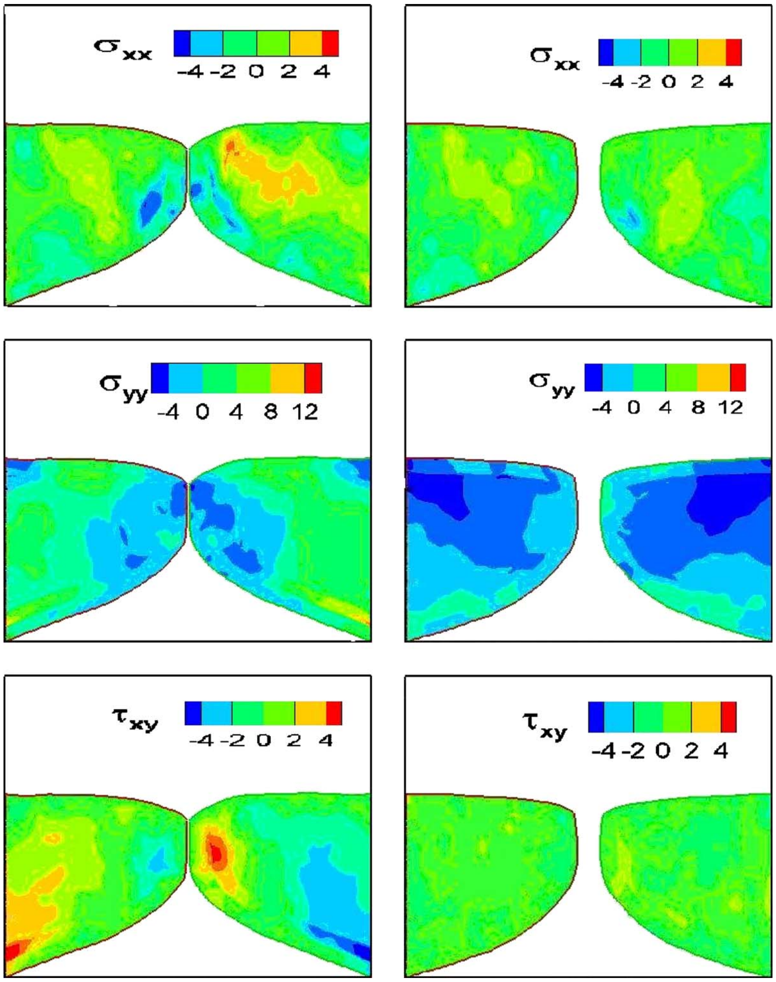

Fig. 9 Contours of stresses (kPa) in the vocal folds during the open and closed phases of the vibration cycle

model does not incorporate all the geometrical and structural complexities of the human larynx, it represents a significant improvement over the 2D model. Similarities between the 2D and 3D geometries employed here also allow us to identify the key effects of the inclusion of three-dimensionality. It should be noted that the 3D model is computationally 30 times more expensive than the 2D model, and this illustrates the challenge associated with these simulations (Fig. 10).

This 3D simulation are carried out on 128 processors on an IBM iDataPlex cluster with Intel(R) Xeon(R) 2.66 GHz processors using and continued until the vocal fold vibration reached a stationary state with a limit-cycle type vibration behavior. Each vibration cycle requires 45 h of CPU time on 128 processors. Figure 12 shows the time history of the glottal airflow volume flux for six vocal fold vibration cycles. The average and peak volume fluxes are 118 ml/s and 300 ml/s, which are inline with in vivo measurement of excised larynges [43]. The Reynolds number based on the peak volume flux rate is 209. The vibration frequency is 242 Hz, which leads to vibration period about 0.00413 s. If we define T as the period of vibration cycle, the maximum flow rate occurs at about $0.4T$ (Fig. 11).

Particular focus with this simulation is to determine the extent to which the inclusion of three-dimensionality affects the glottal jet. Figure 12(*a*) shows an isosurface of the swirl strength [48], which is used to identify vortex structures in flows. The plots indicate that the glottal jet becomes highly three-dimensional in a very early stage in its formation. The three-dimensionality in the

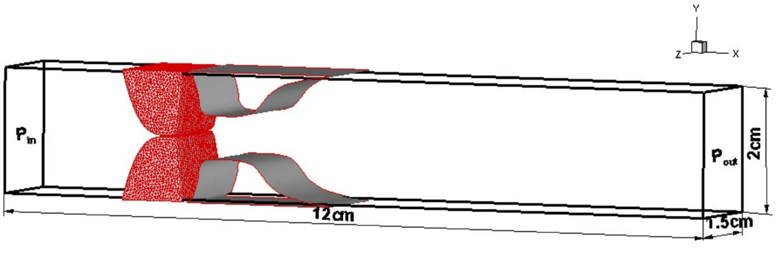

Fig. 10 Flow domain in the 3D flow-structure simulation and finite-element mesh for the true vocal folds

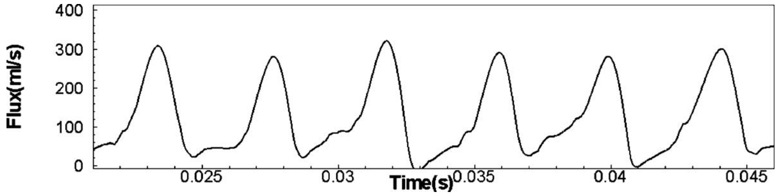

Fig. 11 Time variation of three-dimensional glottal volume flux in the stationary vibration stage

glottal jet amplifies further as the jet develops into the supraglottal region and is characterized by a complex conglomeration of vortex structures. The development of these three-dimensional vortex structures is the first stage in the transition to turbulence of the glottal jet. As shown in the 2D simulation and other PIV experiments [44–46], the glottal jet exhibits a “bimodal behavior,” which has a prominent effect on flow impedance, turbulent characteristics, and vocal fold vibrations. This bimodal phenomenon can also be clearly observed in this 3D simulation. In the particular cycles shown in Fig. 13(*c*), once the jet flow exits the glottis, it starts to deflect toward the lower false vocal fold (shown in Fig. 13(*d*)). In subsequent cycles, the jet stochastically deflects toward one or the other false vocal folds.

To investigate the turbulence characteristics of the glottal jet,

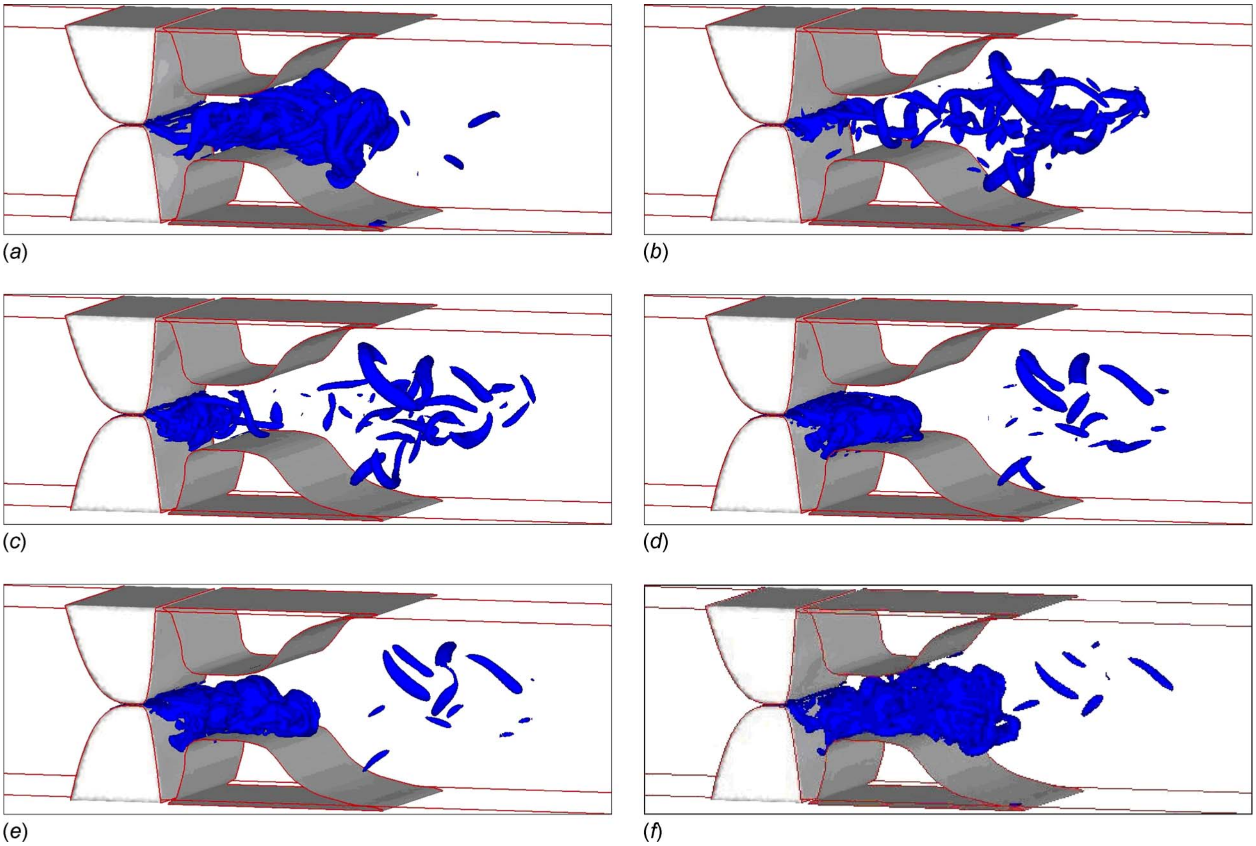
(*a*)
(*b*)
(*c*)
(*d*)
(*e*)
(*f*)

Fig. 12 Isosurface of swirl strength at six different time instants over one vocal fold vibration cycle: (*a*) 0.0245 s, (*b*) 0.02625 s, (*c*) 0.02695 s, (*d*) 0.02765 s, (*e*) 0.02800 s, and (*f*) 0.02870 s

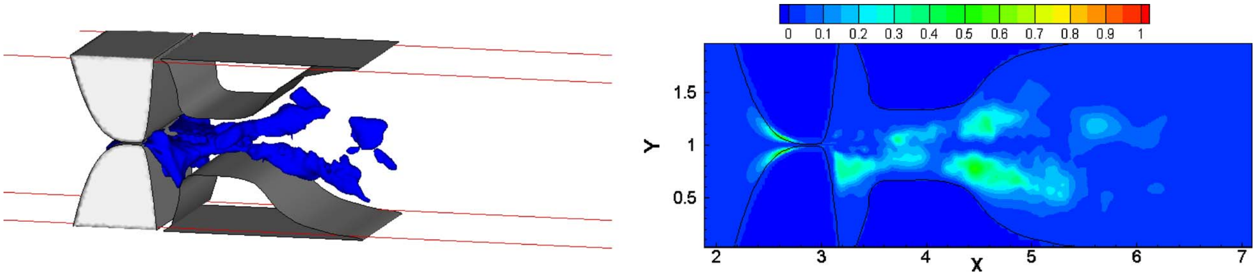

Fig. 13 Isosurface of the turbulent kinetic energy corresponding to a value of $K_T=0.15$ and a contour of turbulent kinetic energy at the center plane ($z=0.75$ cm)

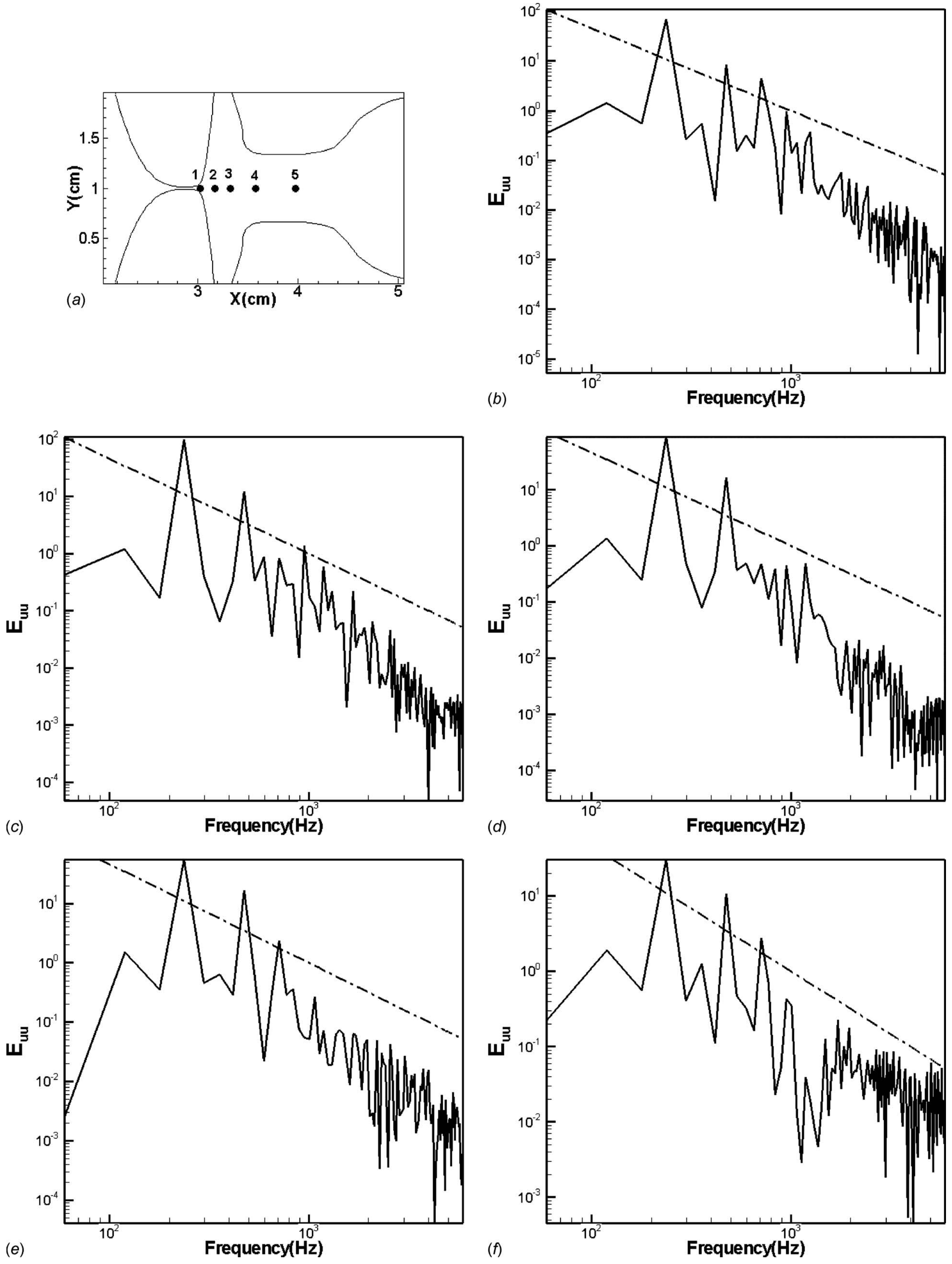

Fig. 14 (*a*) Five locations along the center line in *X*-*Y* plane chosen to perform the flow spectrum analysis. ((*b*)–(*f*)) Span-averaged streamwise velocity spectra: (*b*) point 1 ($x=3.025$ cm), (*c*) point 2 ($x=3.175$ cm), (*d*) point 3 ($x=3.325$ cm), (*e*) point 4 ($x=3.575$ cm), and (*f*) point 5 ($x=3.975$ cm). Dash-dot line ----------- corresponds to $k^{-5/3}$.

we plot the distribution of the turbulence kinetic energy K_T in Fig. 13. The turbulence kinetic energy is computed as

$$K_T = \frac{1}{U_{\text{jet}}^2} \frac{1}{2m\tau} \int_t^{t+m\tau} V_i' V_i' dt \tag{22}$$

where τ is the vibration period, m is the number of cycles over which averaging is done, $V_i' = V_i - \widetilde{U}_i$ denotes the turbulent fluctuation of velocity, V_i denotes the instantaneous velocity, $\widetilde{U}_i$ is the phase-averaged velocity [49,50] (which is 47 m/s for the current simulation), and U_{jet} is the peak jet velocity during the cycle. It should be noted that K_T contains the effects of both the turbulent fluctuation, as well as the cycle-to-cycle deflection of jet. The distribution of the turbulent kinetic energy shows that the turbulence intensity is high in the region just downstream of the glottis and this is due to the rapid breakdown of the jet into small scale vortex structures. In addition, K_T also shows two lobes downstream of the false vocal folds, which are likely due to the jet deflection. The peak value of the turbulent kinetic energy is found to be 0.545.

In order to further understand the transition to turbulence in the glottal jet, we examine the frequency spectra of the velocity in the jet core. Past experiments [45] indicate that the glottal jet has a laminar core, which rapidly transits to turbulence further downstream. We have computed the frequency spectra at the five locations along the center line (shown in Fig. 14(*a*)). The spectra are also averaged along the spanwise direction in the core of the glottal jet.

Also plotted in the spectra is a line with a slope of $-5/3$, which represents the inertial subrange. The plots in Figs. 14(*b*)–14(*f*) show the clearest presence of a substantial inertial subrange at location 4, indicating that the transition to turbulence occurs between locations 3 and 4. Thus, the current simulations allow us to capture the phenomenon of transition to turbulence in the glottal jet.

8 Conclusions

A flow-structure interaction method has been developed, which couples a sharp-interface IBM with a finite-element method based solid dynamics solver. The coupled method provides robust and high-fidelity solution for a highly complex FSI system such as involving three-dimensional flows and viscoelastic solids. The FSI solver is used to simulate flow-induced vibrations of the vocal folds during phonation. Both two- and three-dimensional models have been examined and qualitative and quantitative comparisons with established results indicate that the solver is able to reproduce the salient features of phonatory dynamics. To our knowledge, this is the first time a computational model has been used to capture the phenomena of transition in the glottal jet. The solver is currently being used for detailed investigation of the dynamics in a realistic 3D laryngeal model and these results will be presented in the near future.

Acknowledgment

The project described was supported by Grant No. ROlDC007125 from the National Institute on Deafness and Other Communication Disorders (NIDCD). This research was also supported in part by the National Science Foundation through TeraGrid Resources provided by NICS under Grant No. TG-CTS100002.

References

[1] Dumont, K., Stijnen, J. M. A., Vierendeels, J., van de Vosse, F. N., and Verdonck, P. R., 2004, "Validation of a Fluid-Structure Interaction Model of a Heart Valve Using the Dynamic Mesh Method in Fluent," Comput. Methods Biomech. Biomed. Eng., **7**(3), pp. 139–146.

[2] Einstein, D. R., Kunzelman, K. S., Reinhall, P. G., Nicosia, M. A., and Cochran, R. P., 2005, "Non-Linear Fluid-Coupled Computational Model of the Mitral Valve," J. Heart Valve Dis., **14**(3), pp. 376–385.

[3] Einstein, D. R., del Pin, F., Kunzelman, K., Xiangmin, J., Kuprat, A. P., Carson, J. P., Guccione, J. M., and Ratcliffe, M. B., 2010, "Fluid-Structure Interactions of the Mitral Valve and Left Heart: Comprehensive Strategies, Past, Present and Future," Int. J. Numer. Methods Biomed. Eng., **26**, pp. 348–380.

[4] Guivier, C., Deplano, V., and Pibarot, P., 2007, "New Insights Into the Assessment of the Prosthetic Valve Performance in the Presence of Subaortic Stenosis Through a Fluid-Structure Interaction Model," J. Biomech., **40**(10), pp. 2283–2290.

[5] Kaminsky, R., Dumont, K., Weber, H., Schroll, M., and Verdonck, P., 2007, "PIV Validation of Blood-Heart Valve Leaflet Interaction Modeling," Int. J. Artif. Organs, **30**(7), pp. 640–648.

[6] Morsi, Y. S., Yang, W. W., Wong, G. S., and Das, S., 2007, "Transient Fluid-Structure Coupling for Simulation of a Trileaflet Heart Valve Using Weak Coupling," Int. J. Artif. Organs, **10**(2), pp. 96–103.

[7] Weinberg, E. J., and Kaazempur Mofrad, M. R., 2007, "Transient, Three-Dimensional, Multiscale Simulations of the Human Aortic Valve," Cardiovasc. Eng., **7**(4), pp. 140–155.

[8] Peskin, C. S., 1972, "Flow Patterns Around Heart Valve: A Digital Computer Method for Solving the Equations of Motion," Ph.D. thesis, Albert Einstein College of Medicine, Bronx, NY.

[9] Borazjani, R., Ge, L., and Sotiropoulos, F., 2008, "Curvilinear Immersed Boundary Method for Simulating Fluid Structure Interaction With Complex 3D Rigid Body," J. Comput. Phys., **227**, pp. 7587–7620.

[10] De Hart, J., Peters, G. W., Schreurs, P. J., and Baaijens. F. P., 2003, "A Three-Dimensional Computational Analysis of Fluid-Structure Interaction in the Aortic Valve," J. Biomech., **36**(1), pp. 103–112.

[11] Mittal, R., and Iaccarino, G., 2005, "Immersed Boundary Methods," Annu. Rev. Fluid Mech., **37**, pp. 239–261.

[12] van Loon, R., Anderson, P. D., and, van de Vosse, F. N., 2006, "A Fluid–Structure Interaction Method With Solid-Rigid Contact for Heart Valve Dynamics," J. Comput. Phys., **217**(2), pp. 806–823.

[13] van Loon, R., Anderson, P. D., de Hart, J., and Baaijens, F. P. T., 2004, "A Combined Fictitious Domain/Adaptive Meshing Method for Fluid-Structure Interaction in Heart Valves," Int. J. Numer. Methods Fluids, **46**(5), pp. 533–544.

[14] Watton, P., Luo, X. Y., Yin, M., Bernacca, G. M., and Wheatley, D. J., 2008, "Effect of Ventricle Motion on the Dynamic Behavior of Chorded Mitral Valves," J. Fluids Struct., **24**, pp. 58–74.

[15] Watton, P. N., Luo, X. Y., Wang, X., Bernacca, G. M., Molloy, P., and Wheatley, D. J., 2007, "Dynamic Modelling of Prosthetic Chorded Mitral Valves Using the Immersed Boundary Method," J. Biomech., **40**(3), pp. 613–626.

[16] Mittal, R., Dong, H., Bozkurttas, M., Najjar, F. M., Vargas, A., and von Loebbecke, A., 2008, "A Versatile Sharp Interface Method for Incompressible Flows With Complex Boundaries," J. Comput. Phys., **227**(10), pp. 4825–4852.

[17] Luo, H., Mittal, R., Zheng, X., Bielamowicz, S. A., Walsh, R. J., and Hahn, J. K., 2008, "An Immersed-Boundary Method for Flow-Structure Interaction in Biological Systems With Application to Phonation," J. Comput. Phys., **227**, pp. 9303–9332.

[18] Zhao, H., Freund, J. B., and Moser, R. D., 2008, "A Fixed-Mesh Method of for Incompressible Flow-Structure Systems With Finite Solid Deformations," J. Comput. Phys., **227**, pp. 3114–3140.

[19] Hirano, M., 1977, "Structure and Vibratory Behavior of the Vocal Folds," *Dynamic Aspect of Speech Production*, University of Tokyo Press, Tokyo, Japan.

[20] Belytschko, T., Liu, W., and Moran, B., 2000, *Nonlinear Finite Elements for Continua and Structures*, Wiley, New York.

[21] Van Kan, J., 1986, "A Second-Order Accurate Pressure-Correction Scheme for Viscous Incompressible Flow," SIAM J. Sci. Stat. Comput., **7**(3), pp. 870–891.

[22] Udaykumar, H. S., Mittal, R., Pampunggoon, P., and Khanna, A., 2001, "A Sharp Interface Cartesian Grid Method for Simulating Flows With Complex Moving Boundaries," J. Comput. Phys., **174**, pp. 345–380.

[23] Fung, Y. C., 1993, *Biomechanics*, 2nd ed., Springer-Verlag, New York.

[24] Cuthill, E., and McKee, J., 1969, "Reducing the Bandwidth of Sparse Symmetric Matrices," Proceedings of the 24th National Conference ACM, pp. 157–172.

[25] Gibbs, N. E., Poole, W. G., and Stockmeyer, P. K., 1976, "A Comparison of Several Bandwidth and Profile Reduction Algorithms," ACM Trans. Math. Softw., **2**(4), pp. 322–330.

[26] Zheng, X., 2009, "Biomechanical Modeling of Glottal Aerodynamics and Vocal Fold Vibration During Phonation," Ph.D. thesis, The George Washington University, Washington, DC.

[27] Ghias, R., Mittal, R., and Dong, H., 2007, "A Shape Interface Immersed Boundary Method for Compressible Viscous Flow," J. Comput. Phys., **225**(1), pp. 528–553.

[28] Batchelor, G. K., 2000, *An Introduction to Fluid Dynamics*, Cambridge University Press, Cambridge, UK.

[29] Ishizaka, K., and Flanagan, J. L., 1972, "Synthesis of Voiced Sounds From a Two-Mass Model of the Vocal Cords," Bell Syst. Tech. J., **51**(6), pp. 1233–1268.

[30] Ishizaka, K., 1981, "Equivalent Lumped-Mass Models of Vocal Fold," *Vocal Fold Physiology*, University of Tokyo Press, Tokyo, Japan, pp. 231–241.

[31] Story, B. H., and Titze, I. R., 1995, "Voice Simulation With a Body-Cover Model of the Vocal Folds," J. Acoust. Soc. Am., **97**(2), pp. 1249–1260.

[32] Titze, I. R., 1973, "The Human Vocal Cords: A Mathematical Model: Part I," Phonetica, **28**, pp. 129–170.

[33] Guo, C.-G., and Scherer, R. C., 1993, "Finite Element Simulation of Glottal Flow and Pressure," J. Acoust. Soc. Am., **94**(2), pp. 688–700.

[34] Zhang, C., Zhao, W., Frankel, S., and Mongeau, L., 2002, "Computational Aeroacoustics of Phonation, Part II: Effects of Flow Parameters and Ventricular Folds," J. Acoust. Soc. Am., **112**(5), pp. 2147–2154.

[35] Zhao, W., Zhang, C., Frankel, S., and Mongeau, L., 2002, "Computational Aeroacoustics of Phonation, Part I: Computational Methods and Sound Generation Mechanisms," J. Acoust. Soc. Am., **112**(5), pp. 2134–2146.

[36] Alipour, F., Berry, D. A., and Titze, I. R., 2000, "A Finite-Element Model of Vocal-Fold Vibration," J. Acoust. Soc. Am., **108**(6), pp. 3003–3012.

[37] Cook, D. D., Nauman, E., and Mongeau, L., 2008, "Reducing the Number of Vocal Fold Mechanical Tissue Properties: Evaluation of the Incompressibility and Planar Displacement Assumptions," J. Acoust. Soc. Am., **124**(6), pp. 3888–3896.

[38] Tao, C., and Zhang, Y., Hottinger, D. G., and Jiang, J. J., 2007,"Asymmetric Airflow and Vibration Induced by the Coanda Effect in a Symmetric Model of the Vocal Folds," J. Acoust. Soc. Am., **122**(4), pp. 2270–2278.

[39] Zheng, X., Bielamowicz, S., Luo, H., and Mittal, R., 2009, "Computational Study of the Effect of False Vocal Folds on Glottal Flow on Vocal Fold Vibration During Phonation," Ann. Biomed. Eng., **37**(3), pp. 625–642.

[40] Herzel, H., Berry, D., and Titze, I. R., 1994, "Analysis of Vocal Disorders With Methods From the Nonlinear Dynamics," J. Speech Hear. Res., **37**, pp. 1008–1019.

[41] Baer, T., 1975, "Investigation of Phonation Using Excised Larynges," Ph.D. thesis, Massachusetts of Technology, Cambridge, MA.

[42] Titze, I. R., Schmidt, S. S., and Titze, M. R., 1995, "Phonation Threshold Pressure in a Physical Model of the Vocal Fold Mucosa," J. Acoust. Soc. Am., **97**(5), pp. 3080–3084.

[43] Alipour, F., Jaiswal, S., and Finnegan, E., 2007, "Aerodynamic and Acoustic Effects of False Vocal Folds and Epiglottis in Excised Larynx Models," Ann. Otol. Rhinol. Laryngol., **116**(2), pp. 135–144.

[44] Erath, B. D., and Plesniak, M. W., 2006, "An Investigation of Bimodal Jet Trajectory in Flow Through Scaled Models of the Human Vocal Tract," Exp. Fluids, **40**, pp. 683–696.

[45] Neubauer, J., and Zhang, Z., 2007, "Coherent Structures of the Near Field Flow in a Self-Oscillating Physical Model of the Vocal Folds," J. Acoust. Soc. Am., **121**(2), pp. 1102–1118.

[46] Triep, M., Brücker, Ch., and Schröder, W., 2005, "High-Speed PIV Measurements of the Flow Downstream of a Dynamic Mechanical Model of the Human Vocal Folds," Exp. Fluids, **39**, pp. 232–245.

[47] Titze, I. R., 1994, "Mechanical Stress in Phonation," J. Voice, **8**(2), pp. 99–105.

[48] Chong, M. S., and Perry, A. E., 1990, "A General Classification of Three-Dimensional Flow Fields," Phys. Fluids A, **2**, pp. 765–777.

[49] Hussain, A. K. M. F., and Reynolds, W. C., 1975, "Measurements in Fully Developed Turbulent Channel Flow," ASME J. Fluids Eng., **97**, pp. 568–580.

[50] Mittal, R., Simmons, S. P., and Najjar, F., 2003, "Numerical Study of Pulsatile Flow in a Constricted Channel," J. Fluid Mech., **485**, pp. 337–378.